**ARL**

**US Army Research Laboratory**

# Visualizing Energy on Target: Molecular Dynamics Simulations

**by DeCarlos E Taylor**

**NOTICES**

**Disclaimers**

The findings in this report are not to be construed as an official Department of the Army position unless so designated by other authorized documents.

Citation of manufacturer's or trade names does not constitute an official endorsement or approval of the use thereof.

Destroy this report when it is no longer needed. Do not return it to the originator.

US Army Research Laboratory

# Visualizing Energy on Target: Molecular Dynamics Simulations

**by DeCarlos E Taylor**
*Weapons and Materials Research Directorate, ARL*

| REPORT DOCUMENTATION PAGE | | *Form Approved* *OMB No. 0704-0188* |
|---|---|---|

Public reporting burden for this collection of information is estimated to average 1 hour per response, including the time for reviewing instructions, searching existing data sources, gathering and maintaining the data needed, and completing and reviewing the collection information. Send comments regarding this burden estimate or any other aspect of this collection of information, including suggestions for reducing the burden, to Department of Defense, Washington Headquarters Services, Directorate for Information Operations and Reports (0704-0188), 1215 Jefferson Davis Highway, Suite 1204, Arlington, VA 22202-4302. Respondents should be aware that notwithstanding any other provision of law, no person shall be subject to any penalty for failing to comply with a collection of information if it does not display a currently valid OMB control number.
**PLEASE DO NOT RETURN YOUR FORM TO THE ABOVE ADDRESS.**

| 1. REPORT DATE *(DD-MM-YYYY)* | 2. REPORT TYPE | 3. DATES COVERED (From - To) |
|---|---|---|
| December 2017 | Technical Report | 1 October 2015–30 September 2016 |

| 4. TITLE AND SUBTITLE | 5a. CONTRACT NUMBER |
|---|---|
| Visualizing Energy on Target: Molecular Dynamics Simulations | |
| | 5b. GRANT NUMBER |
| | 5c. PROGRAM ELEMENT NUMBER |
| 6. AUTHOR(S) | 5d. PROJECT NUMBER |
| DeCarlos E Taylor | |
| | 5e. TASK NUMBER |
| | 5f. WORK UNIT NUMBER |

| 7. PERFORMING ORGANIZATION NAME(S) AND ADDRESS(ES) | 8. PERFORMING ORGANIZATION REPORT NUMBER |
|---|---|
| US Army Research Laboratory<br>ATTN: RDRL-WML-B<br>Aberdeen Proving Ground, MD 21005-5069 | ARL-TR-8234 |

| 9. SPONSORING/MONITORING AGENCY NAME(S) AND ADDRESS(ES) | 10. SPONSOR/MONITOR'S ACRONYM(S) |
|---|---|
| | |
| | 11. SPONSOR/MONITOR'S REPORT NUMBER(S) |

**12. DISTRIBUTION/AVAILABILITY STATEMENT**
Approved for public release; distribution is unlimited.

**13. SUPPLEMENTARY NOTES**

**14. ABSTRACT**
In this work, using atomistic molecular dynamics simulation, the mechanism of energy deposition by a shocked diatomic gas into a stationary target is studied as a function of multiple variables including gas density, impact velocity, and target rigidity. The work focuses on the resulting gas dynamics and details the partitioning of the energy among the available rotational and vibrational channels as a function of impact condition. The results suggest that rotational excitations are important at all impact velocities and that vibrational excitation in the gas is only important for high-velocity impacts. The results also suggest that the rate of energy deposition into the vibrational channels of the gas is a function of the density.

**15. SUBJECT TERMS**
molecular dynamics, energy deposition, rovibrational, partitioning, simulation

| 16. SECURITY CLASSIFICATION OF: | | | 17. LIMITATION OF ABSTRACT | 18. NUMBER OF PAGES | 19a. NAME OF RESPONSIBLE PERSON<br>DeCarlos E Taylor |
|---|---|---|---|---|---|
| a. REPORT | b. ABSTRACT | c. THIS PAGE | UU | 30 | 19b. TELEPHONE NUMBER (Include area code)<br>410-306-0853 |
| Unclassified | Unclassified | Unclassified | | | |

# Contents

## List of Figures

## List of Tables

## Acknowledgments

This work was supported in part by a grant of computer time from the Department of Defense High Performance Computing Modernization Program at the US Army Research Laboratory Supercomputing Resource Center.

## 1. Introduction

The mechanism and rate of vibrational energy transfer in gas–surface collisions has been of great interest both experimentally and theoretically. Experimentally,[1,2] it has been observed that accommodation coefficients for high-frequency molecular vibrations tend to be small, whereas corresponding coefficients for molecules with low-frequency vibrations close to the impact surface are comparatively much higher (although some exceptions have been reported[3]). Theoretically, gas–surface interactions have been studied using a variety of simulation techniques. Alexander et al.[4] employed a scattering model to study energy transfer for atoms impacting self-assembled monolayer surfaces. Lucchese and Tully[5] employed a stochastic trajectory approach to study the impact of nitric oxide molecules on the 001 surface of the lithium fluoride crystal as a function of vibrational frequency, surface temperature, and translational energy. In that work, it was found that the dominant mechanism of energy transfer between the surface and impacting gas was coupling of vibrations to surface phonons and that a relatively small amount of energy resulted from repartitioning of the vibrational energy in rotational and translation modes.

In this work, using atomistic molecular dynamics (MD) simulation, the mechanism of energy deposition by a shocked diatomic gas (nitrogen [$N_2$]) into a stationary target is studied as a function of multiple variables including gas density, impact velocity, and target rigidity. We focus here primarily on the resulting gas dynamics and detail the partitioning of the energy among the available rotational and vibrational channels as a function of impact condition. The results suggest that rotational excitations are important at all impact velocities and that vibrational excitation in the gas is only important for high-velocity impacts. The results also suggest that the rate of energy deposition into the vibrational channels of the gas is a function of the density.

## 2. Computational Methods

### 2.1 Simulation Cell

A general schematic of the simulation cells used in this work is shown in Fig. 1. Each cell consists of a target placed on the left side of the cell and a diatomic gas ($N_2$) occupying the right side of the cell where the Z Cartesian axis is normal to the target surface as shown. The cell dimensions for all simulations were $100.8 \times 100.8 \times 820$ Å.
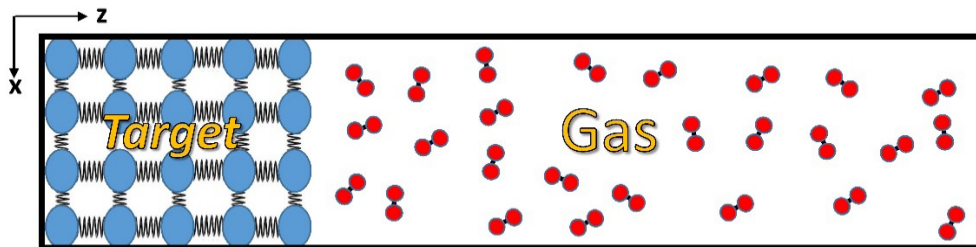
**Fig. 1     Schematic of simulation cell (image not drawn to scale)**

For each simulation, the target consisted of point masses (14.0 g/mol) with an inter-particle separation of 1.2 Å. The target layers were regularly spaced from Z = 0 to Z = 14.4 Å yielding 91,728 particles in the target region of the simulation cell. Each pair of atoms in the target was connected by springs to all its nearest neighbors and interacted via a harmonic potential

$$V(r)_{target} = \frac{1}{2}k(r - r_o)^2, \tag{1}$$

where $r$ is the inter-particle separation (bonded interactions only) and $r_o$ is the equilibrium bond length. In this work, the parameter $r_o$ equaled 1.2 Å, which is equivalent to the value of the lattice spacing used to construct the target layers. Therefore, the particles in the target already occupied their equilibrium lattice positions, by construction, and as a result, there was minimal reorientation of the particles in the target layer during cell equilibration. The uniformity of the target layer geometry, irrespective of target rigidity (to be discussed), is important since this removes a potential source of variation in the observed energy deposition and gas dynamics as the impact conditions are varied.

The force constant $k$ in Eq. 1 controls the strength of the interaction between bonded pairs and consequently determines the target stiffness. Six targets were prepared with force constant values of 100, 500, 1500, 3000, 6000, and 10,000 (kcal mol$^{-1}$ Å$^{-2}$) and as a rough estimate of the surface stiffness for each $k$, one can compute the vibrational frequency between a pair of target particles acting as harmonic oscillators that are decoupled from their other neighbors. In this approximation, the frequency, $v$, between each target atom pair is given by

$$v = \frac{1}{2\pi}\sqrt{\frac{k}{\mu}}, \tag{2}$$

where $\mu$ is the reduced mass between the particles and $k$ is the force constant value for the target. The resulting frequencies for the 6 force constants used in this work are given in Table 1. The frequencies range from a low energy mode of 410 cm$^{-1}$

(characteristic of a relatively soft target) up to a maximum of 4100 cm$^{-1}$, a high-energy vibration characteristic of a rigid target.

**Table 1   Vibrational frequencies, $v$, for each force constant $k$. Frequencies in cm$^{-1}$, force constants in kcal mol$^{-1}$ Å$^{-2}$.**

| $k$ | $v$ (cm$^{-1}$) |
|------|------|
| 100 | 410 |
| 500 | 917 |
| 1500 | 1588 |
| 3000 | 2246 |
| 6000 | 3176 |
| 10000 | 4100 |

Following placement of the target in the simulation cell, the impacting gas was generated by population of the empty region of the cell above the target with randomly oriented $N_2$ molecules at multiple experimental densities, $\rho$. The experimental density of nitrogen gas is 0.001251 g/cm$^3$.[6] This is a factor of 1000 times lower than the densities of materials (such as energetics with $\rho \approx 1.8$ g/cm$^3$) that are usually studied in atomistic shock simulations. At the experimental density and cell dimensions used in this work (100.8 × 100.8 × 820 Å), only 215 $N_2$ molecules are present in the gas region of the cell (Fig. 2) and it was not expected that any meaningful physics regarding gas dynamics would be observed with this paucity of atoms.
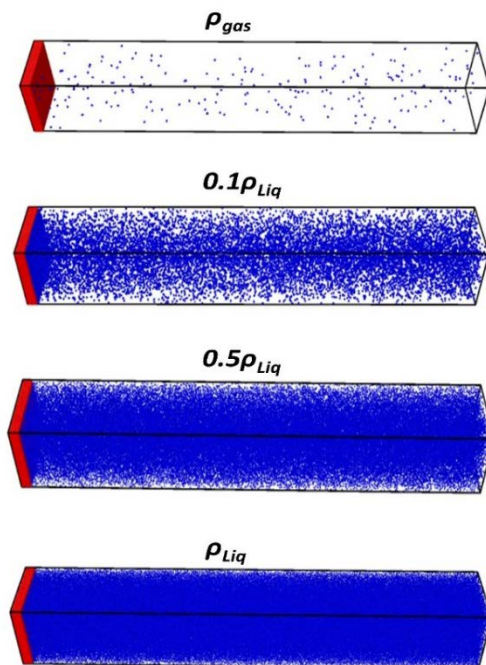


**Fig. 2      Simulation cells with various $N_2$ densities. $N_2$ atoms are blue and the target region is red.**

Due to the low particle count of $N_2$ at the experimental gas density, simulation cells with $N_2$ molecules at the experimental liquid density ($\rho_{Liq} = 0.8084$ g/cm$^3$) were prepared. In addition, simulation cells using values of $0.1\rho_{Liq}$ and $0.5\rho_{Liq}$ were constructed (Fig. 2) to study the effect of $N_2$ density on energy deposition and redistribution. Table 2 lists the total simulation size (including the 91,728 target atoms) as a function of $N_2$ density. The simulation size ranges from 92,158 atoms for the simulation cell at the gas density (consisting almost entirely of target atoms) up to 369,776 atoms for the simulation cell at the full liquid density. Combining the 6 targets with the 4 $N_2$ densities yielded 24 different simulation cells for analysis.

**Table 2   Number of atoms in simulation cell (including target) as function of $N_2$ density**

| $\rho$ | Number of atoms |
|---|---|
| $\rho_{air}$ | 92,158 |
| $0.1\rho_{Liq}$ | 119,380 |
| $0.5\rho_{Liq}$ | 230,752 |
| $\rho_{Liq}$ | 369,776 |

## 2.2  Interaction Potentials

The target-target particle interactions were governed by a harmonic potential (Eq. 1) as previously described. The $N_2$ molecules were treated using the Condensed-phase Optimized Molecular Potentials for Atomistic Simulation Studies (COMPASS)[7] force field where the intramolecular interactions of $N_2$ were given by

$$V(r)_{N_2}^{intra} = c_2(r - b_o)^2 + c_3(r - b_o)^3 + c_4(r - b_o)^4 \qquad (3)$$

and the intermolecular interactions between $N_2$ molecules were of the Lennard-Jones form

$$V(r)_{N_2}^{inter} = \varepsilon\left[2\left(\frac{\sigma}{r}\right)^9 - 3\left(\frac{\sigma}{r}\right)^6\right]. \qquad (4)$$

The parameters appearing in Eqs. 3 and 4 ($c$, $b_o$, $\varepsilon$, $\sigma$) were taken from the literature.[7] The functional form of the nitrogen-target particle interactions can be chosen freely, and for simplicity, these interactions were also represented by Eq. 4 with the same parameter values.

## 2.3  Simulation Protocol

All simulations were run using the Large-scale Atomic/Molecular Massively Parallel Simulator (LAMMPS)[8] software package. Each simulation cell was equilibrated in the isothermal-isochoric (NVT) ensemble for a period of 500 ps

using a 1-fs time step at a temperature (T) of 100 K. The simulation employed periodic boundary conditions in the X and Y directions (Fig. 1) and was nonperiodic along Z. To keep the target region from translating (a necessity for the impact studies), the bottom layer of target atoms at $Z = 0$ was kept fixed during the simulations. Diffusion of the $N_2$ molecules from the "open" end of the simulation cell (upper edge opposite the target) was prevented by using the "wall/reflect" option in LAMMPS. With this technique, if a nitrogen atom crossed the upper cell boundary by a distance $\Delta$, it was placed back inside the cell by the same $\Delta$ and the sign of the Z-component of the velocity for that particle was flipped, thereby confining all atoms to the interior of the cell.

After equilibration, $N_2$ was driven into the target at multiple impact velocities, $v_{imp}$. Momentum of $N_2$ toward the target was introduced by addition of $v_{imp}$ to the Z-component of the velocity vector, $v_z$, for each nitrogen atom. The values of $v_x$ and $v_y$ were unchanged. For each of the 24 simulation cells, 4 values of $v_{imp}$ (0.5, 1.0, 1.5, and 2.0 km/s) were used yielding 96 simulations total. For each cell, the impact trajectory was integrated in the microcanonical (NVE) ensemble for a period of 100 ps. However, only the data in the first 40 ps were used for determination of total energy deposition and rovibrational analysis because of the wall/reflect option in LAMMPS as previously described. This option, although useful, represents a perturbation on the translational and rovibrational energies since it alters the molecular geometry and velocities. Observation of the simulation trajectories showed that after driving $N_2$ into the target, the molecules diffused back toward the free end of the cell and reached the upper edge after approximately 40 ps. Therefore, analyses of the gas dynamics were terminated at that point so that the results would not be impacted by the artificial reflections occurring at the far end of the cell.

## 2.4 Energy Deposition into Target

The energy of the target was computed at every simulation step and included kinetic and potential energy contributions where the potential energy of the target was given by summation of Eq. 1 over all bonded pairs in the target region. The energy deposition, $E_{dep}$, is given by

$$E_{dep} = E_{Target,i} - E_{Target,o} \ , \tag{4}$$

where $E_{Target,i}$ is the energy of the compressed target at the $i$th time step and $E_{Target,o}$ is the equilibrium energy of the target before impact. The target energies, $E_{Target,i}$ were computed by averaging over 500 energy values centered about the current time step.

## 2.5  Energy Distribution in N₂

The partitioning of energy in $N_2$ was monitored by computing the kinetic energy of vibration and the kinetic energy of rotation of all $N_2$ molecules. The molecular rovibrational energies were obtained using a postprocessing program, developed by the author, that executes the following steps for each $N_2$ molecule:

1) Compute the center of mass and translate to the origin.

2) Subtract velocity contributions corresponding to center of mass translation.

3) Compute the inertia tensor and diagonalize yielding the principal axes.

4) Rotate the local molecular coordinates (and atomic velocities) of the current molecule to the principal axis orientation using the convention that the eigenvector with a zero moment of inertia (bond axis of a diatomic) is oriented along the X-axis.

5) Compute the kinetic energy of vibration, $K_v = mv_x^2$.

6) Compute the rotational kinetic energy, $K_{rot} = \frac{1}{2}I_y\omega_y^2 + \frac{1}{2}I_z\omega_z^2$, where $Iy$ and $Iz$ are the inertial moments (eigenvalues obtained in step 3) and the angular velocities, $\omega$, about each axis are given by $\frac{v}{r}$ where $v$ is the velocity about the axis and $r$ is the distance of the atom from the origin in the local coordinate system.

## 3.  Results

### 3.1  Energy Deposition

Representative plots of the change in target energy and temperature, relative to the equilibrium state, as a function of impact velocity for the target with $k = 1500$ are presented in Figs. 3–6. As shown, at a fixed density, the energy transferred to the target increases as a function of the impact velocity, as expected. The energy deposition also increases as a function of the density of $N_2$ and after 40 ps, the amount of energy transferred to the target for the $0.5\rho_{Liq}$ and full liquid density $N_2$ simulations is essentially equivalent ($\approx$20,000 kcal/mol). This suggests saturation with respect to density for these small-length scales. The temperature rise of the target ranges from approximately 4 K for impacts of $N_2$ at the gas density to approximately 50 K for simulations at the full liquid density. However, these energy and temperature values correspond to quantities computed 40 ps after impact (the point at which the simulations were terminated due to the issues discussed previously) and the final energy and temperature values could change if

a longer simulation with a larger cell was used. However, based on the slopes of the curves after 40 ps of simulation time, it is not expected that the final energy and temperature would be "significantly" different since the slopes of the curves are approaching zero in most cases.



**Fig. 3    Change in target energy and temperature, relative to the equilibrium state, as a function of impact velocity (km/s) for $k$ = 1500 target and $N_2$ at the experimental gas density**
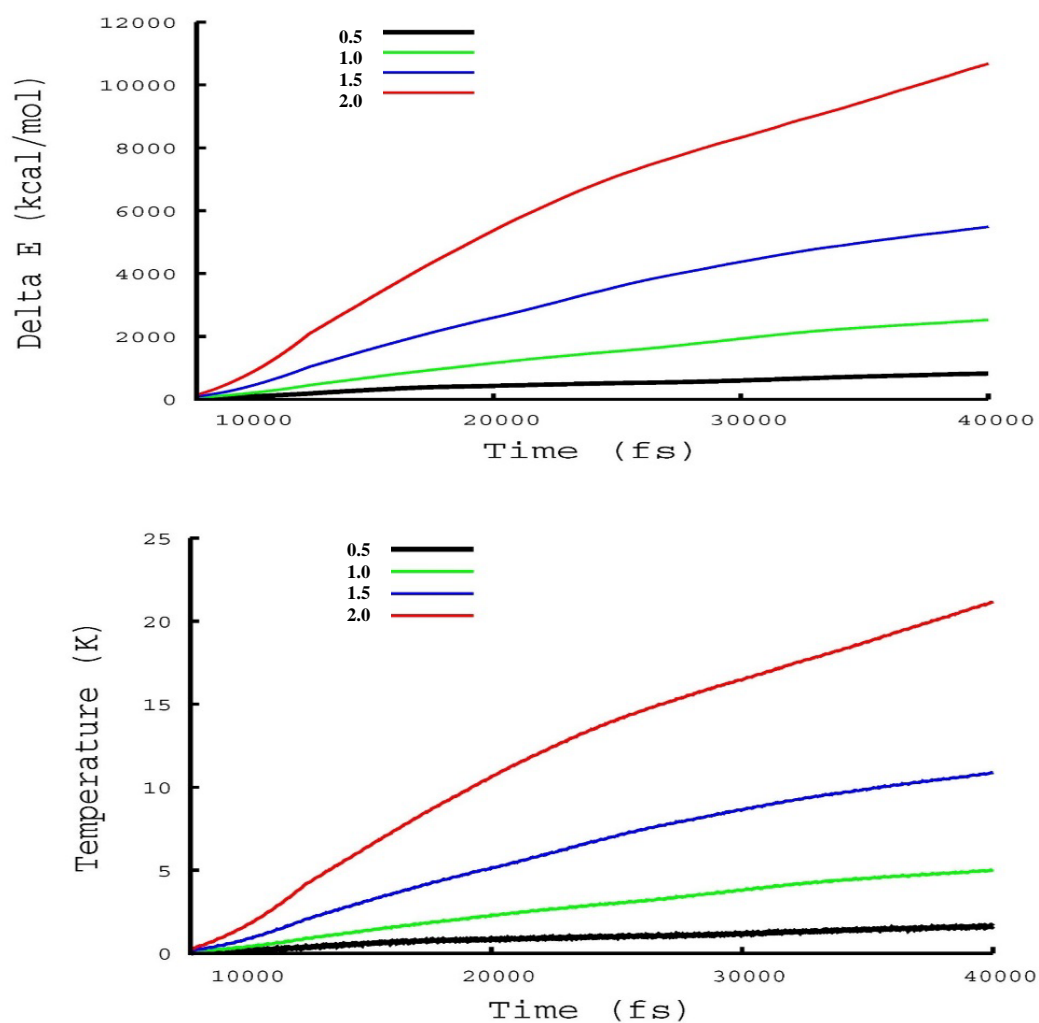
**Fig. 4** **Change in target energy and temperature, relative to the equilibrium state, as a function of impact velocity (km/s) for** $k = 1500$ **target and** $0.1\rho_{Liq}$ **density for** $N_2$
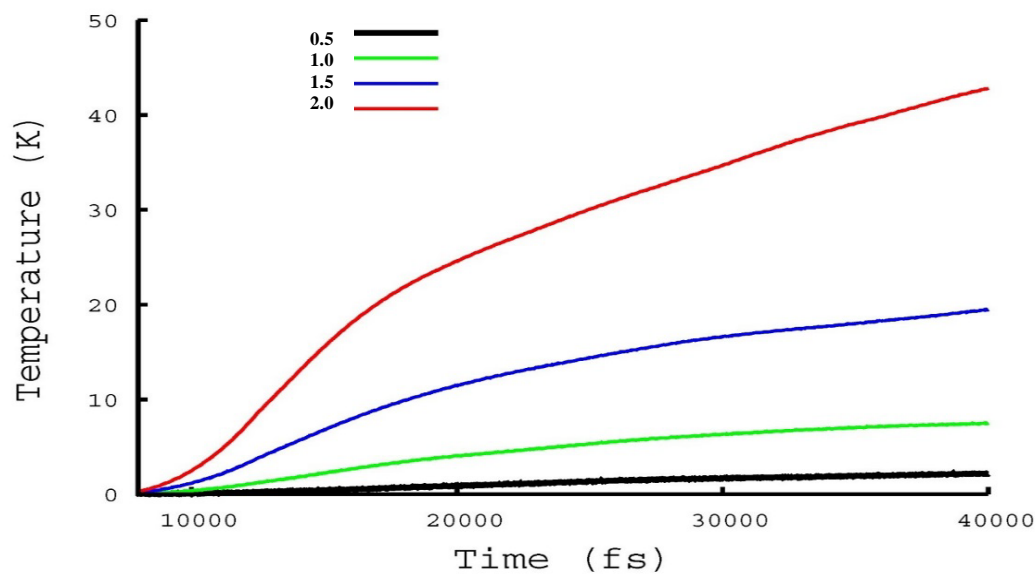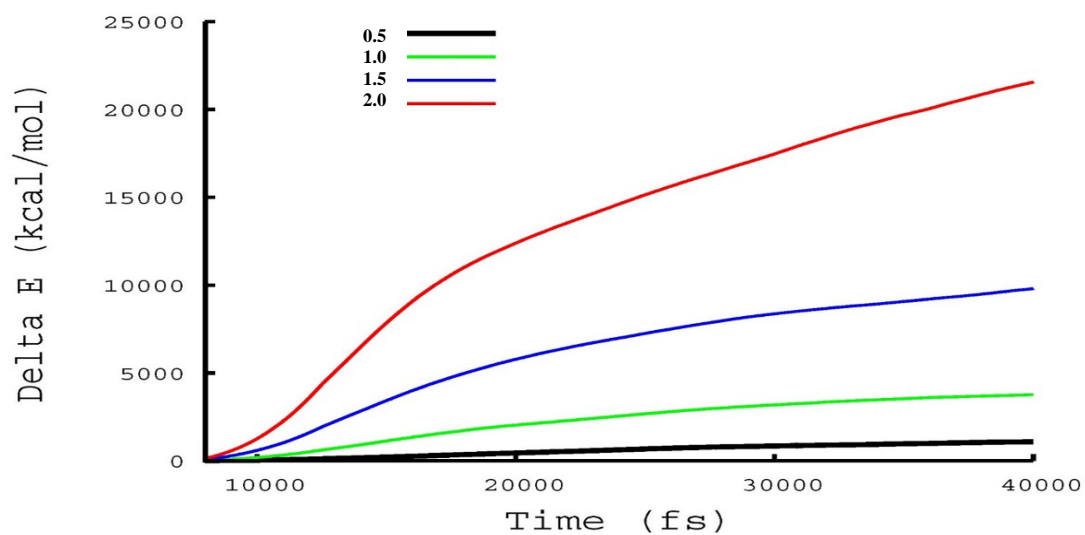
**Fig. 5** **Change in target energy and temperature, relative to the equilibrium state, as a function of impact velocity (km/s) for $k = 1500$ target and $0.5\rho_{Liq}$ density for $N_2$**
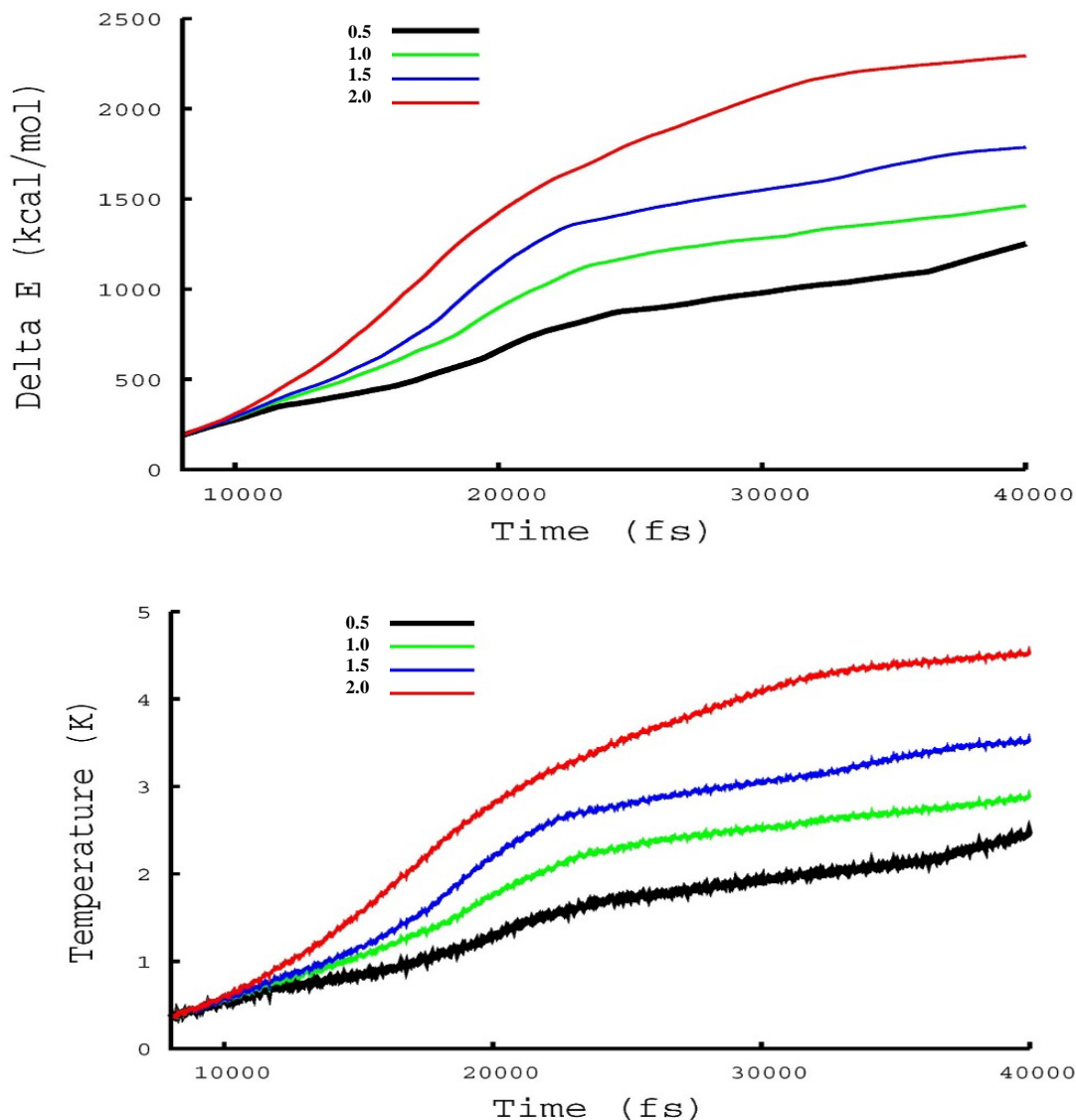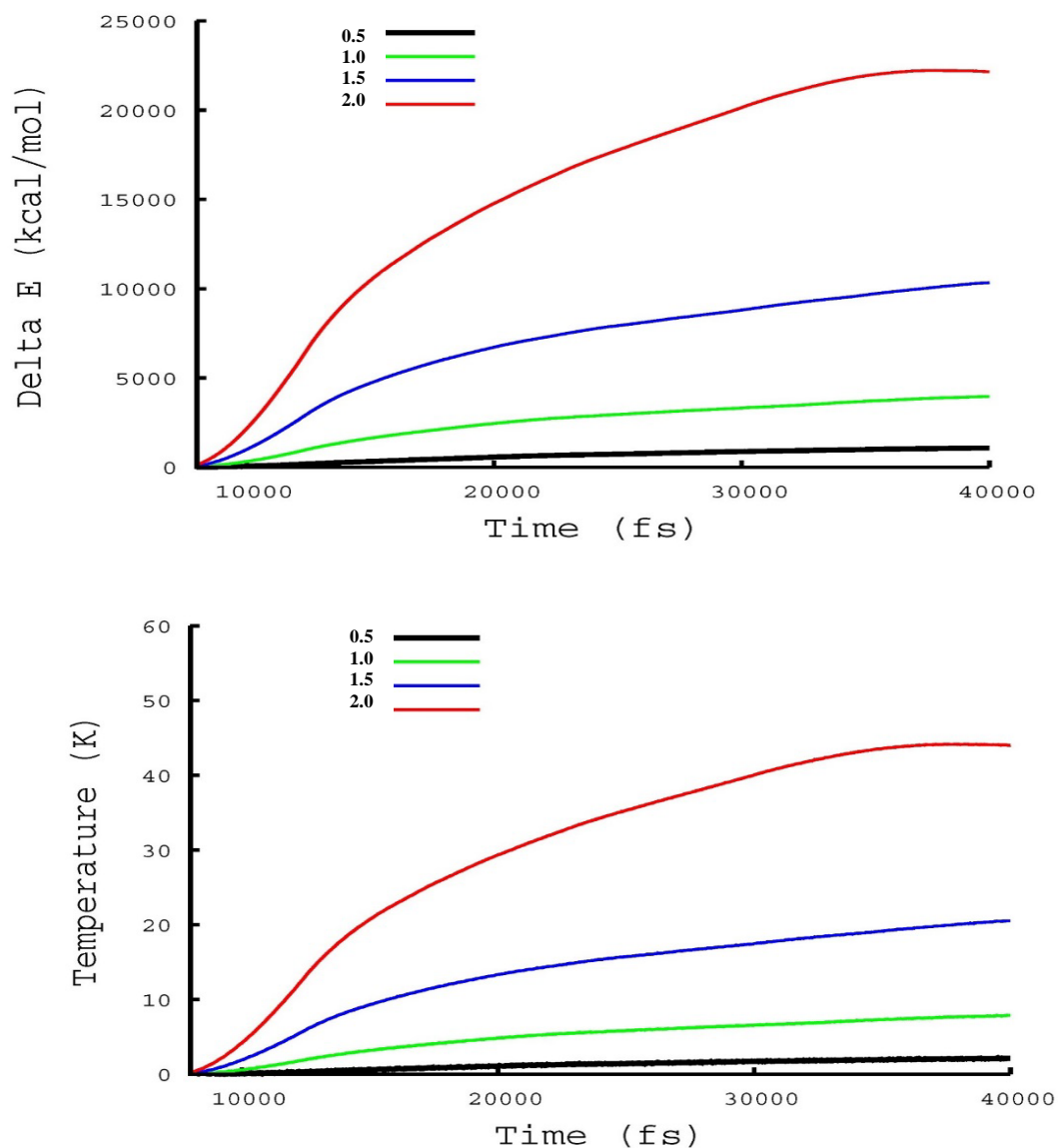
**Fig. 6**     **Change in target energy and temperature, relative to the equilibrium state, as a function of impact velocity (km/s) for $k$ = 1500 target and $\rho_{Liq}$ density for $N_2$**

Tables 3–8 report the energy deposition rate (in units of gigawatts [GW]) per mol) and the associated temperature increase for all 96 combinations of target, $N_2$ density, and impact velocity studied in this work. Examination of the data shows that the energy deposition rate or "power" (energy per unit time) follows anticipated trends. At constant density and constant target stiffness, the power increases as a function of impact velocity. As an example, for the $k$ = 1500 target and $0.5\rho_{Liq}$ $N_2$ density, the power increases from a value of 7.4 GW for $v_{imp}$ = 0.5 km/s to a value of 133.9 GW for $v_{imp}$ = 2.0 km/s. Similarly, at constant impact velocity and constant density, the power decreases as a function of target rigidity. As an example, at

$v_{imp}$ = 2.0 km/s and $0.5\rho_{Liq}$ N$_2$ density, the energy deposition rate decreases from 384 GW for the very soft target ($k$ = 100) to only 61 GW for the very stiff target ($k$ = 10,000) at the same density. Similar trends follow from other target, density, and $v_{imp}$ combinations.

**Table 3   Energy deposition rate into target with $k$ = 100, $V_{imp}$ (km/s), ΔE (kcal/mol), ΔT (K), and rate (GW/mol)**

| | | | | | | | | |
|---|---|---|---|---|---|---|---|---|
| | | | | **$k = 100$** | | | | |
| | **$\rho_{air}$** | | | | | **$0.1\rho_{Liq}$** | | |
| **$v_{imp}$** | **ΔE** | **ΔT** | **Rate** | | **$v_{imp}$** | **ΔE** | **ΔT** | **Rate** |
| 0.5 | 2340.4 | 4.6 | 14.0 | | 0.5 | 2677.8 | 5.3 | 16.0 |
| 1.0 | 2742.9 | 5.4 | 16.4 | | 1.0 | 8201.6 | 16.3 | 49.0 |
| 1.5 | 3306.8 | 6.5 | 19.8 | | 1.5 | 19087.0 | 38.0 | 114.0 |
| 2.0 | 3809.6 | 7.5 | 22.8 | | 2.0 | 36011.0 | 71.6 | 215.2 |
| | **$0.5\rho_{Liq}$** | | | | | **$\rho_{liq}$** | | |
| 0.5 | 3318.1 | 6.7 | 19.8 | | 0.5 | 3387.7 | 6.8 | 20.2 |
| 1.0 | 12876.6 | 25.9 | 76.9 | | 1.0 | 13059.7 | 26.3 | 78.0 |
| 1.5 | 33322.2 | 66.8 | 199.1 | | 1.5 | 32382.3 | 64.9 | 193.5 |
| 2.0 | 64264.0 | 128.2 | 384.0 | | 2.0 | 62777.8 | 125.1 | 375.1 |

**Table 4   Energy deposition rate into target with k = 500, Vimp (km/s), ΔE (kcal/mol), ΔT (K), and rate (GW/mol)**

| | | | | | | | | |
|---|---|---|---|---|---|---|---|---|
| | | | | **$k = 500$** | | | | |
| | **$\rho_{air}$** | | | | | **$0.1\rho_{Liq}$** | | |
| **$v_{imp}$** | **ΔE** | **ΔT** | **Rate** | | **$v_{imp}$** | **ΔE** | **ΔT** | **Rate** |
| 0.5 | 1638.1 | 3.2 | 9.8 | | 0.5 | 1541.6 | 3.0 | 9.2 |
| 1.0 | 2132.1 | 4.2 | 12.7 | | 1.0 | 4617.1 | 9.1 | 27.6 |
| 1.5 | 2386.6 | 4.7 | 14.3 | | 1.5 | 10543.1 | 20.9 | 63.0 |
| 2.0 | 3311.5 | 6.6 | 19.8 | | 2.0 | 19887.7 | 39.4 | 118.8 |
| | **$0.5\rho_{Liq}$** | | | | | **$\rho_{liq}$** | | |
| 0.5 | 1860.1 | 3.6 | 11.1 | | 0.5 | 1772.2 | 3.6 | 10.6 |
| 1.0 | 6777.0 | 13.4 | 40.5 | | 1.0 | 6632.9 | 13.3 | 39.6 |
| 1.5 | 18326.1 | 36.4 | 109.5 | | 1.5 | 17308.6 | 34.5 | 103.4 |
| 2.0 | 37057.2 | 73.5 | 221.4 | | 2.0 | 34683.3 | 68.9 | 207.2 |

**Table 5   Energy deposition rate into targets with *k* = 1500, V$_{imp}$ (km/s), ΔE (kcal/mol), ΔT (K), and rate (GW/mol)**

| | | | | | | | |
|---|---|---|---|---|---|---|---|
| *k = 1500* | | | | | | | |
| ρ$_{air}$ | | | | 0.1ρ$_{Liq}$ | | | |
| V$_{imp}$ | ΔE | ΔT | Rate | V$_{imp}$ | ΔE | ΔT | Rate |
| 0.5 | 1399.6 | 2.8 | 8.4 | 0.5 | 969.8 | 1.9 | 5.8 |
| 1.0 | 1668.6 | 3.3 | 10.0 | 1.0 | 2960.3 | 5.9 | 17.7 |
| 1.5 | 1899.8 | 3.8 | 11.4 | 1.5 | 6463.6 | 12.8 | 38.6 |
| 2.0 | 2404.5 | 4.8 | 14.4 | 2.0 | 12512.8 | 24.8 | 74.8 |
| 0.5ρ$_{Liq}$ | | | | ρ$_{liq}$ | | | |
| 0.5 | 1235.0 | 2.4 | 7.4 | 0.5 | 1210.1 | 2.4 | 7.2 |
| 1.0 | 4311.4 | 8.5 | 25.8 | 1.0 | 4260.2 | 8.5 | 25.5 |
| 1.5 | 11233.0 | 22.3 | 67.1 | 1.5 | 10232.8 | 20.4 | 61.1 |
| 2.0 | 22404.4 | 44.4 | 133.9 | 2.0 | 20931.9 | 41.6 | 125.1 |

**Table 6   Energy deposition rate into targets with *k* = 3000, V$_{imp}$ (km/s), ΔE (kcal/mol), ΔT (K), and rate (GW/mol)**

| | | | | | | | |
|---|---|---|---|---|---|---|---|
| *k = 3000* | | | | | | | |
| ρ$_{air}$ | | | | 0.1ρ$_{Liq}$ | | | |
| V$_{imp}$ | ΔE | ΔT | Rate | V$_{imp}$ | ΔE | ΔT | Rate |
| 0.5 | 877.4 | 1.7 | 5.2 | 0.5 | 861.8 | 1.4 | 5.1 |
| 1.0 | 922.0 | 1.8 | 5.5 | 1.0 | 2255.5 | 4.2 | 13.5 |
| 1.5 | 1338.5 | 2.6 | 8.0 | 1.5 | 4904.8 | 9.4 | 29.3 |
| 2.0 | 1760.6 | 3.4 | 10.5 | 2.0 | 9720.6 | 18.9 | 58.1 |
| 0.5ρ$_{Liq}$ | | | | ρ$_{liq}$ | | | |
| 0.5 | 777.6 | 1.7 | 4.6 | 0.5 | 786.2 | 1.3 | 4.7 |
| 1.0 | 3410.3 | 6.9 | 20.4 | 1.0 | 3407.9 | 6.6 | 20.4 |
| 1.5 | 8661.7 | 17.3 | 51.8 | 1.5 | 8141.2 | 16.0 | 48.6 |
| 2.0 | 17421.2 | 34.6 | 104.1 | 2.0 | 16278.1 | 32.2 | 97.3 |

**Table 7   Energy deposition rate into targets with *k* = 6000, V$_{imp}$ (km/s), ΔE (kcal/mol), ΔT (K), and rate (GW/mol)**

| | | | | | | | |
|---|---|---|---|---|---|---|---|
| *k = 6000* | | | | | | | |
| ρ$_{air}$ | | | | 0.1ρ$_{Liq}$ | | | |
| V$_{imp}$ | ΔE | ΔT | Rate | V$_{imp}$ | ΔE | ΔT | Rate |
| 0.5 | 820.7 | 1.6 | 4.9 | 0.5 | 368.2 | 0.7 | 2.2 |
| 1.0 | 843.8 | 1.7 | 5.0 | 1.0 | 1208.3 | 2.4 | 7.2 |
| 1.5 | 1067.1 | 2.1 | 6.4 | 1.5 | 3191.1 | 6.3 | 19.1 |
| 2.0 | 1218.9 | 2.4 | 7.3 | 2.0 | 6633.8 | 13.1 | 39.6 |
| 0.5ρ$_{Liq}$ | | | | ρ$_{liq}$ | | | |
| 0.5 | 317.8 | 0.7 | 1.9 | 0.5 | 213.3 | 0.4 | 1.3 |
| 1.0 | 1936.5 | 3.9 | 11.6 | 1.0 | 1762.5 | 3.5 | 10.5 |
| 1.5 | 6364.2 | 12.7 | 38.0 | 1.5 | 6295.8 | 12.5 | 37.6 |
| 2.0 | 13559.3 | 26.9 | 81.0 | 2.0 | 12824.4 | 25.4 | 76.6 |

**Table 8  Energy deposition rate into targets with $k$ = 10,000, $V_{imp}$ (km/s), $\Delta E$ (kcal/mol), $\Delta T$ (K), and rate (GW/mol)**

| | | | | $k = 10,000$ | | | | |
|---|---|---|---|---|---|---|---|---|
| | $\rho_{air}$ | | | | | $0.1\rho_{Liq}$ | | |
| $v_{imp}$ | $\Delta E$ | $\Delta T$ | Rate | | $v_{imp}$ | $\Delta E$ | $\Delta T$ | Rate |
| 0.5 | 457.6 | 0.9 | 2.7 | | 0.5 | 150.3 | 0.3 | 0.9 |
| 1.0 | 627.7 | 1.2 | 3.8 | | 1.0 | 553.7 | 1.1 | 3.3 |
| 1.5 | 669.8 | 1.3 | 4.0 | | 1.5 | 1842.9 | 3.6 | 11.0 |
| 2.0 | 917.9 | 1.8 | 5.5 | | 2.0 | 4222.5 | 8.3 | 25.2 |
| | $0.5\rho_{Liq}$ | | | | | $\rho_{liq}$ | | |
| 0.5 | 92.9 | 0.2 | 0.6 | | 0.5 | 39.5 | 0.1 | 0.2 |
| 1.0 | 828.4 | 1.6 | 4.9 | | 1.0 | 690.0 | 1.4 | 4.1 |
| 1.5 | 3887.8 | 7.7 | 23.2 | | 1.5 | 3697.6 | 7.4 | 22.1 |
| 2.0 | 10235.4 | 20.3 | 61.2 | | 2.0 | 10328.3 | 20.5 | 61.7 |

## 3.2  Energy Redistribution in Gas

Plots of the molecular vibrational and rotational kinetic energies, summed over all $N_2$ molecules in the cell, for the $0.1\rho_{Liq}$, $0.5\rho_{Liq}$, and $\rho_{Liq}$ densities ($k = 1500$ target) are presented in Figs. 7–9. These plots are representative of the results obtained for all other target, density, and $v_{imp}$ combinations except those for the experimental gas density that were indeterminate due to the low number of $N_2$ molecule. As such, this experimental density is not discussed further. As shown, for each density, the vibrational kinetic energy remains essentially constant (thermal oscillations aside) for the 3 lowest $v_{imp}$ values suggesting that for these weaker impacts, there is no appreciable change in vibrational energy within the 40-ps time frame of these simulations. However, for $v_{imp} = 2$ km/s, there is a marked increase in the kinetic energy of vibration suggesting that there is an impact threshold upon which vibrational excitation (either via direct energy deposition or through rovibrational coupling) becomes important.
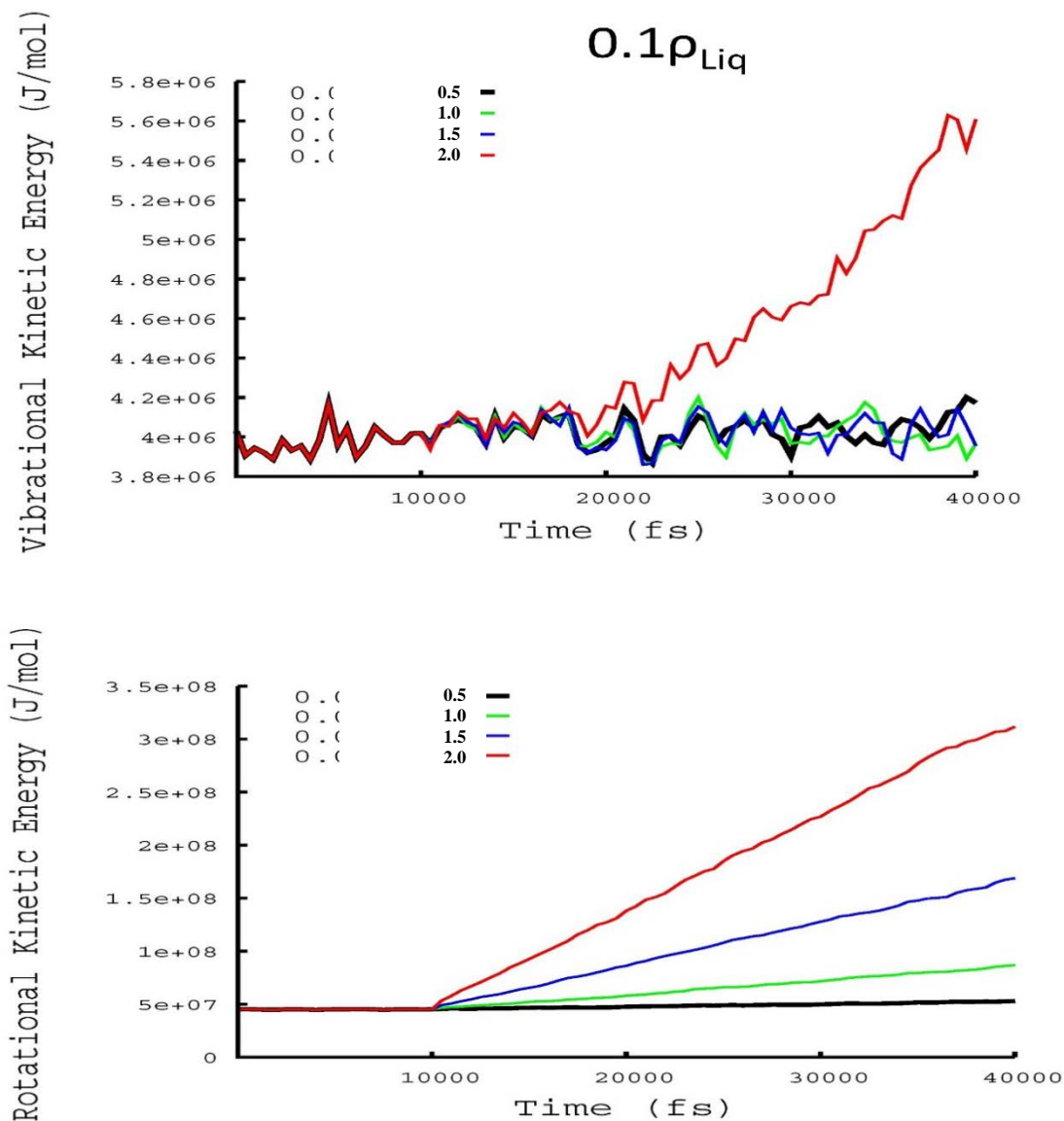
**Fig. 7      Total rotational and vibrational kinetic energies for $k = 1500$ target and $0.1\rho_{Liq}$ $N_2$ density as a function of impact velocity (km/s)**
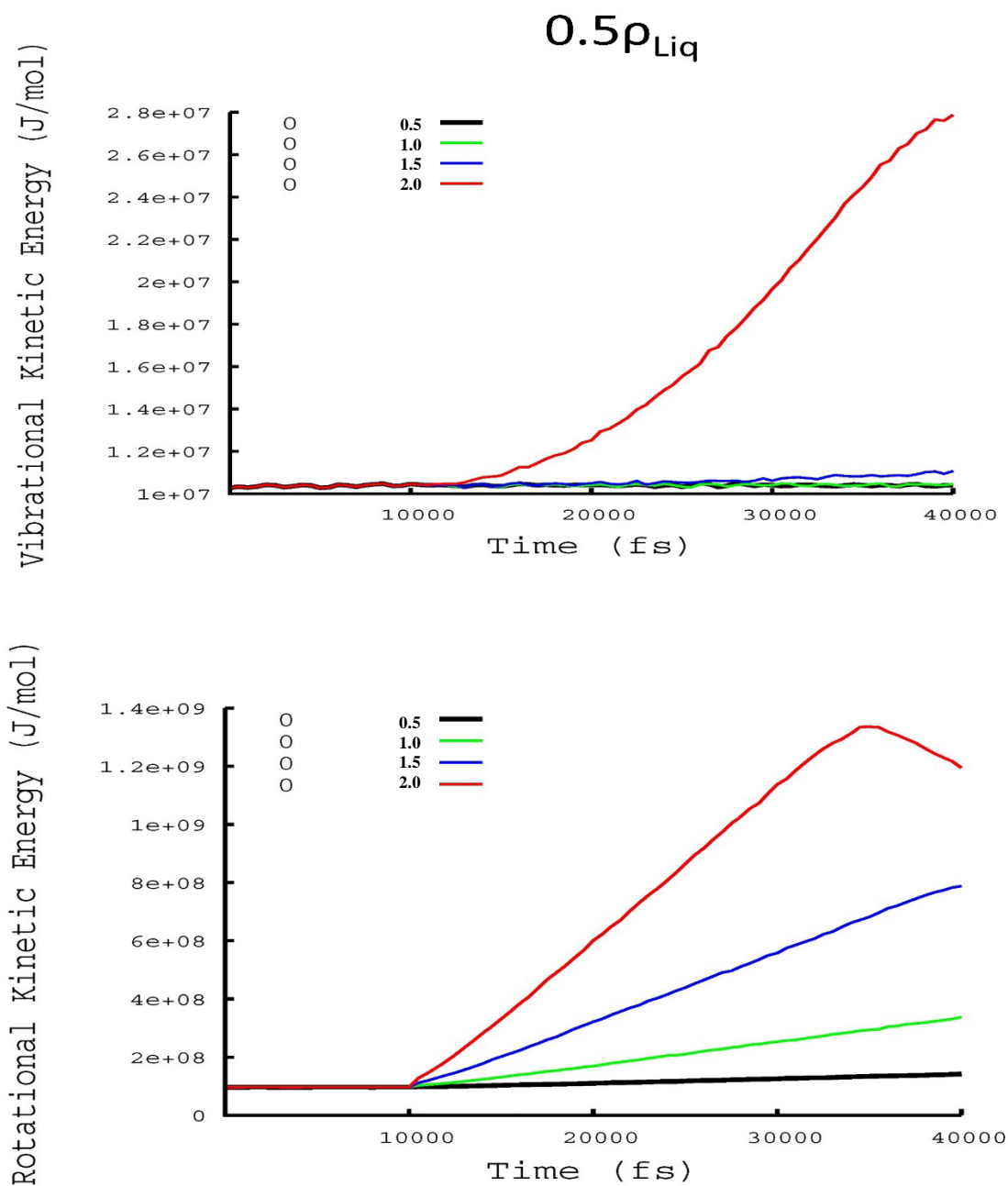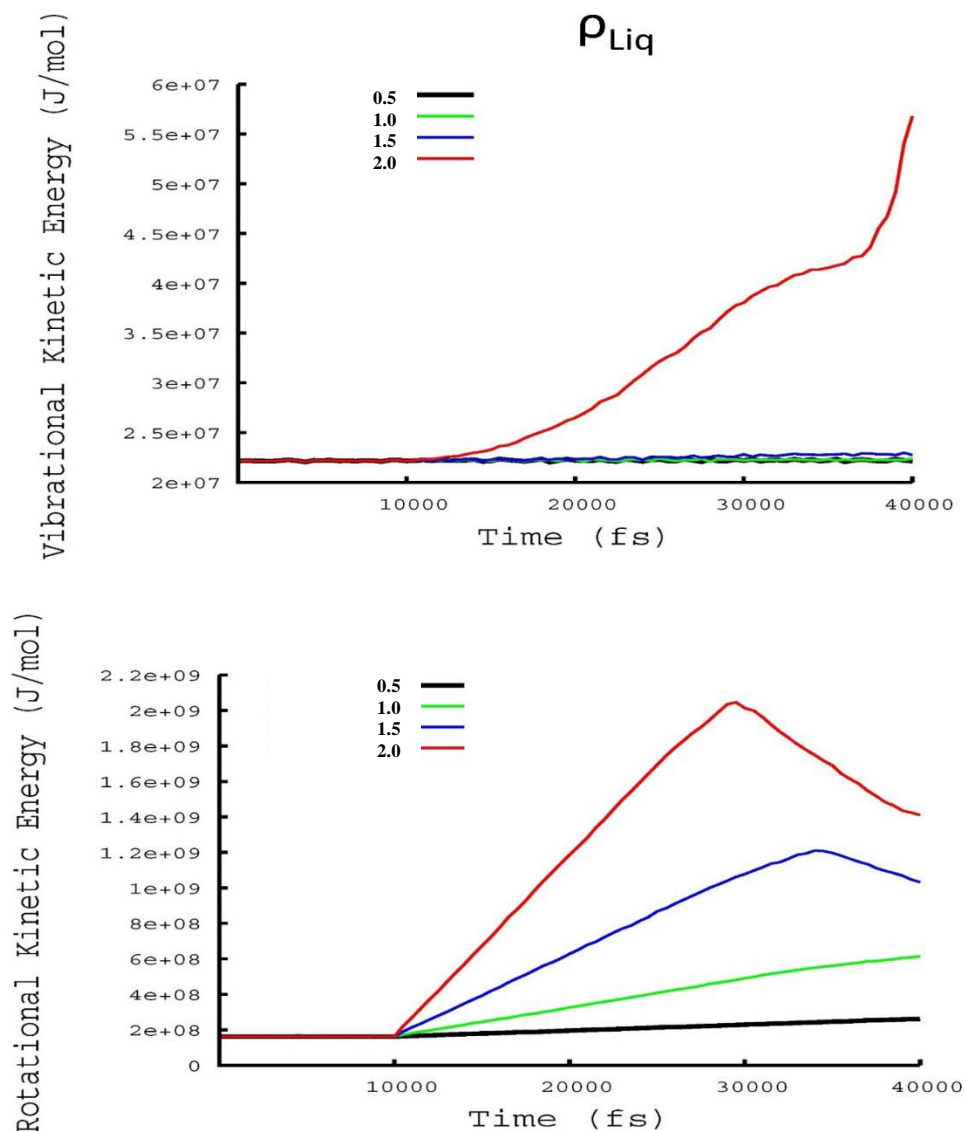
**Fig. 8** **Total rotational and vibrational kinetic energies for** *k* **= 1500 target and 0.5ρ$_{Liq}$ N$_2$ density as a function of impact velocity (km/s)**

**Fig. 9** **Total rotational and vibrational kinetic energies for _k_ = 1500 target and ρ_Liq N₂ density as a function of impact velocity (km/s)**

The data represented in Figs. 7–9 also suggest that the rate of energy transfer into the vibrational modes is a function of the density. In each figure, the impact portion of the simulation begins at 10 ps with the steps prior to that representing the final steps of the equilibration phase. For the $0.1\rho_{Liq}$ density simulation (Fig. 7), the vibrational kinetic energy for $v_{imp} = 2$ km/s begins to increase at approximately 20 ps (i.e., 10 ps after the initial impact). The increase occurs at approximately 12 ps for the $0.5\rho_{Liq}$ simulation (Fig. 8) (i.e., 2 ps after impact), and at full density (Fig. 9) the kinetic energy increase begins almost instantaneously. On the contrary, the rotational kinetic energy for all impact and density values shows an

instantaneous increase immediately after target impact at t = 10 ps, as one would expect, since rotation is a much lower energy process than vibration. The change in rotational kinetic energy for $v_{imp}$ = 0.5 km/s is much less than that observed for the higher impact velocities (masked in part by the scale of the plot). This is due to the reduced number of $N_2$ collisions with the target resulting from this comparatively weak value of $v_{imp}$.

Figures 10–12 are renderings of the simulation cell containing the $k$ = 1500 target ($v_{imp}$ = 1.5 km/s) where the local regions of the cell are colored by the average rovibrational temperature per $N_2$ molecule. In the figures, the target is represented by the plane of atoms at the far left edge of the cell and each colored bin is of dimension 5 × 5 × 15 Å. The bins in the target region remain "cold" in the renderings since the rovibrational analysis was limited to the $N_2$ region of the cell. The times used to label the snapshots in each figure are relative to the start of the impact. At t = 0 (no impact), the rovibrational energy is equally distributed throughout $N_2$ with an average rovibrational temperature of approximately 100 K per local bin. However, the snapshots taken 2.5 ps after impact show an increase in the rovibrational temperature at the interface, and the radial extent of this "hot spot" appears to increase as a function of the $N_2$ density. At t = 25 ps, the gas reaches its maximum compression and begins to flow back down the tube, remaining rovibrationally hot through t = 40 ps at which point the simulation trajectory was terminated. Figures 10–12 also suggest that the internal temperature of $N_2$ after impact is a function of density. For the $0.1\rho_{Liq}$ density simulation (Fig. 10), molecular internal temperatures exceed 1000 K (red bins) after impact. However, when the density is increased to $0.5\rho_{Liq}$ and $\rho_{Liq}$, the molecular temperatures only rise to approximately 500 K and 300 K, respectively. This is likely attributable to an increased level of energy dissipation occurring after impact between the $N_2$ molecules that results from the increased number of intermolecular interactions at the higher mass densities. This may also be why the size of the hot spot increases with density.
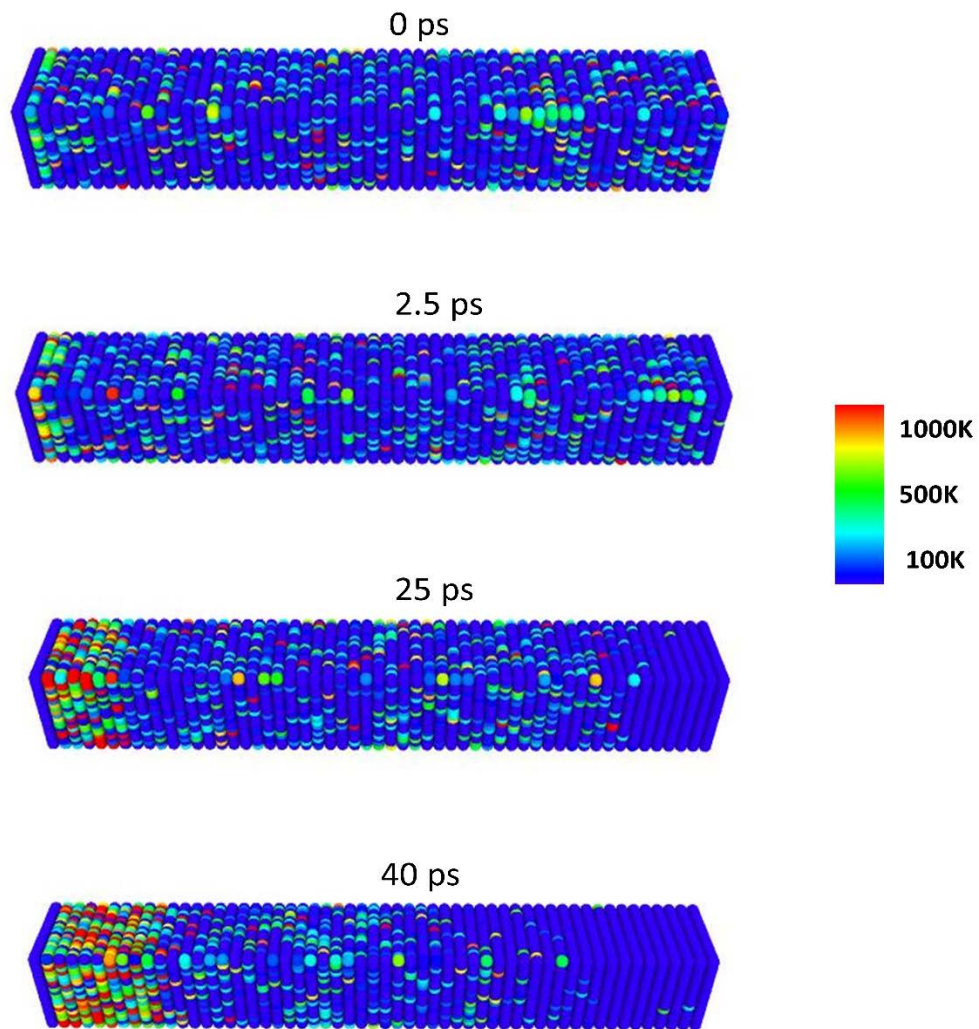
**0 ps**

**2.5 ps**

1000K
500K
100K

**25 ps**

**40 ps**

**Fig. 10    Local rovibrational temperatures for 0.1ρ$_{Liq}$ N$_2$ density. Times measured relative to start of impact. Target is at far left of cell.**

**Fig. 11   Local rovibrational temperatures for 0.5ρ$_{Liq}$ N$_2$ density. Times measured relative to start of impact. Target is at far left of cell.**

19

**Fig. 12    Local rovibrational temperatures for $\rho_{Liq}$ $N_2$ density. Times measured relative to start of impact. Target is at far left of cell.**

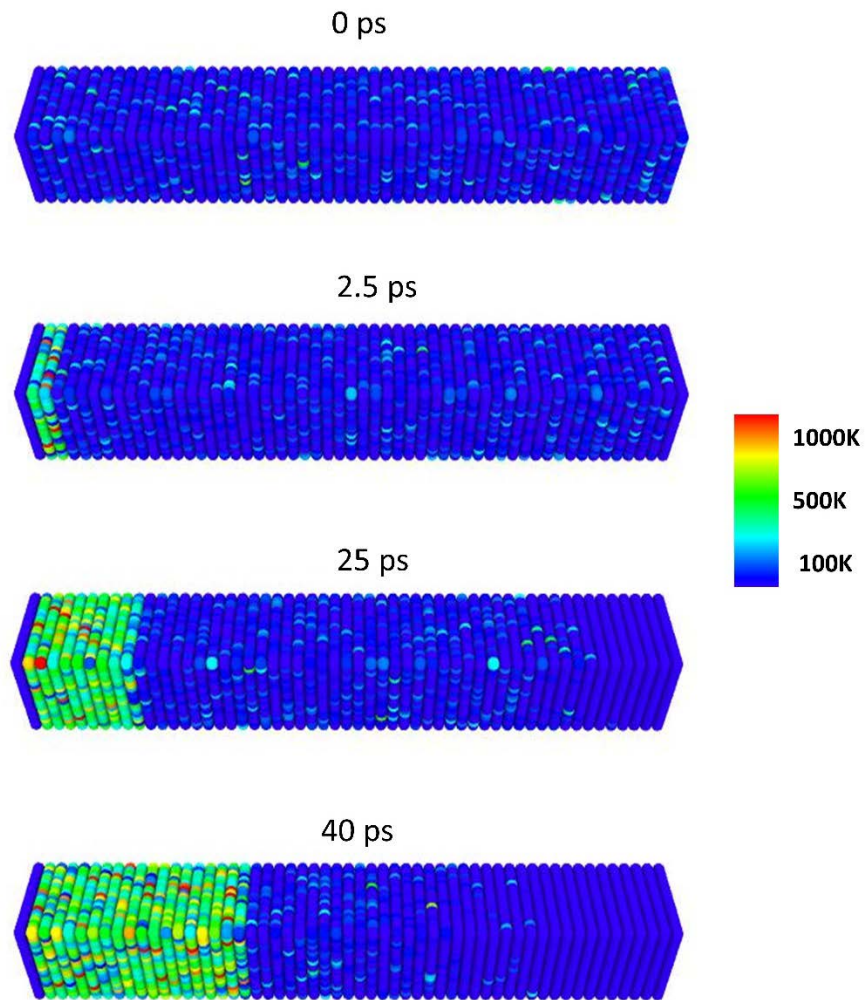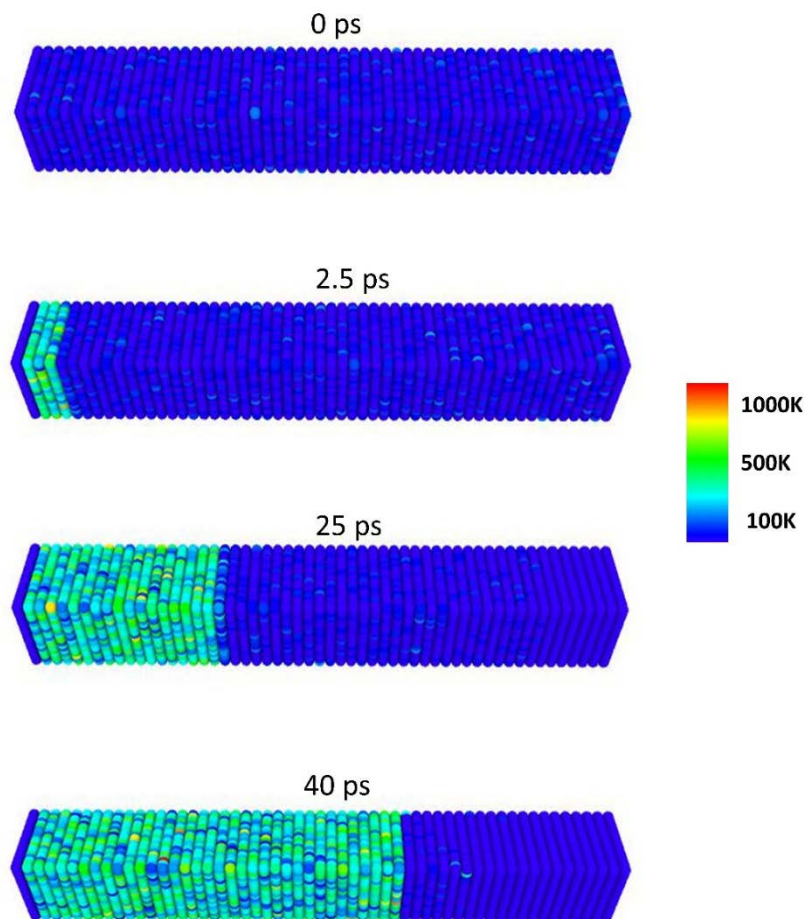## 4. Conclusion

In this work, the physics of energy deposition and rovibrational excitation was studied using MD simulation. The results suggest that rotational excitations are important at all impact velocities. However, vibrational excitation is only important for high-velocity impacts (2 km/s for the systems in this work). The results also suggest that the rate of energy deposition into the vibrational channels is a function of the density. The simulations conducted in this work used nonreactive potentials. However, for the lower density simulations, internal particle temperatures exceeded 1000 K, which in principle could drive molecular dissociation that may influence the observed mechanisms of energy transfer. Although the simulation sizes used in this work are beyond the application of quantum mechanical approaches, the available empirical models that include chemical reactivity (at increased computational expense, however) may provide insight regarding the importance of bond dissociation and ionization on energy deposition and partitioning.

## 5. References

1. Rosenblatt G. Translational and internal energy accommodation of molecular gases with solid surfaces. Acc Chem Res. 1981;14:42–48.

2. Foner SN, Hudson RL. Vibrationally excited nitrogen molecules formed in the catalytic decomposition of ammonia on platinum. J Chem Phys. 1984;80(1):518–523.

3. Zacharias H, Loy MMT, Roland PA. Scattering of vibrationally excited NO off LiF and $CaF_2$ surfaces. Phys Rev Lett. 1982;49(24):1790–1794.

4. Alexander WA, Zhang J, Murray WJ, Nathanson GM, Minton TK. Kinematics and dynamics of atomic-beam scattering on liquid and self-assembled monolayer surfaces. Far Disc. 2012;157:355–374.

5. Lucchese RR, Tully JC. Trajectory studies of vibrational energy transfer in gas–surface collisions. J Chem Phys. 1984;80:3451–3462.

6. The Engineering ToolBox. Gases – density. [accessed 2017 Oct 25] http://www.engineeringtoolbox.com/gas-density-d_158.html.

7. Yang J, Tian A, Sun H. COMPASS force field for 14 inorganic molecules, He, Ne, Ar, Kr, Xe, $H_2$, $O_2$, $N_2$, NO, CO, $CO_2$, $NO_2$, $CS_2$, and $SO_2$, in liquid phases. J Phys Chem B. 2000;104:4951–4957.

8. Plimpton S. Fast parallel algorithms for short–range molecular dynamics. J Comp Phys. 1995;117:1–42.

| | |
|---|---|
| 1 (PDF) | DEFENSE TECHNICAL INFORMATION CTR DTIC OCA |
| 2 (PDF) | DIR ARL IMAL HRA RECORDS MGMT RDRL DCL TECH LIB |
| 1 (PDF) | GOVT PRINTG OFC A MALHOTRA |
| 1 (PDF) | ARMY RESEARCH OFC J PARKER |
| 22 (PDF) | ARL RDRL WM B FORCH RDRL WML N TRIVEDI RDRL WML B D TAYLOR B RICE E BYRD W MATTSON J CIEZAK-JENKINS T JENKINS F DELUCIA J GOTTFRIED R PESCE-RODRIGUEZ S WEINGARTEN I BATYREV B BARNES R SAUSA A BESTE RDRL WML C S AUBERT K MCNESBY G SUTHERLAND RDRL WML D R BEYER J VEALS M MCQUAID |